ACS APPLIED MATERIALS & INTERFACES

www.acsami.org

Research Article

Elucidating the Spatial Dynamics of Charge Carriers in Quasi-Two-Dimensional Perovskites

Dohyung Kim* and Mahshid Ahmadi*

Cite This: https://doi.org/10.1021/acsami.1c07876

Read Online

ACCESS | Metrics & More | Article Recommendations | Supporting Information

ABSTRACT: Quasi-two dimensional (2D) organic–inorganic hybrid perovskites (OIHPs) have shown better ambient stability with decent solar cell performances. However, the power conversion efficiency of quasi-2D OIHPs is still below that of 3D polycrystalline perovskites. To understand the limitation of quasi-2D OIHPs, we explore charge carrier properties in 3D and quasi-2D perovskites using advanced scanning probe microscopy techniques. Kelvin probe force microscopy (KPFM) identifies slow degradation in quasi-2D perovskites by measuring photovoltage variations under thermal and humid conditions. Bias-driven photocurrent maps obtained by conductive-atomic force microscopy (c-AFM) measurements reveal local inhomogeneous conduction and hysteretic currents in quasi-2D perovskites while relatively uniform conductivity is observed on individual grains in the 3D perovskite counterparts. In addition, bias-driven KPFM and *I*–*V* measurements in the lateral Au electrode devices show higher charge carrier dynamics with stronger potential drop at the interfaces in the 3D perovskite than those of the quasi-2D perovskite devices. The combination of c-AFM and KPFM results confirm less ionic conduction in the quasi-2D perovskites as compared to the 3D perovskites. Our study elucidates underlying mechanisms behind the lower efficiency of quasi-2D perovskites, which is necessary for further development of efficient and stable perovskite-based devices.

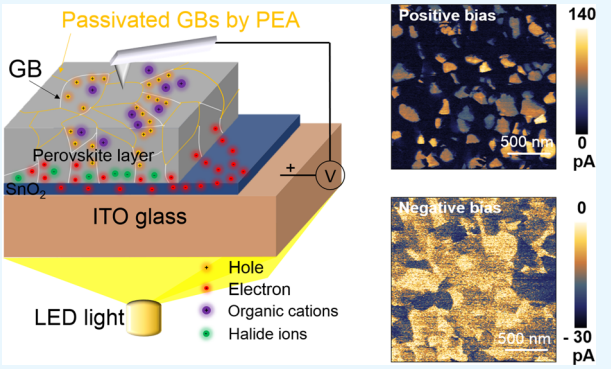

KEYWORDS: *quasi-2D, mixed perovskite, PEA incorporation, charge carriers, KPFM, c-AFM*

INTRODUCTION

Organic–inorganic hybrid perovskites (OIHPs) with three-dimensional (3D) structures have been developed rapidly due to their outstanding photophysical properties and versatility for various potential applications including photovoltaics,[1] photodetectors,[2] and light-emitting diodes (LEDs).[3] Particularly, compositional engineering of OIHPs with double cations [CH_3NH_3 (methylammonium, MA) and $HC(NH_2)_2$ (formamidinium, FA)] and double halides (I and Br), for example, $85FAPBI_3$-$15MAPbBr_3$, has led to higher efficiencies and better stability.[4−6]

For 3D perovskite optoelectronics, thermal and humidity-induced instability is a bottleneck for commercialization. Specifically, moisture can permeate through the film surface along with grain boundaries (GBs) and contribute to degradation of the films,[7,8] resulting in decomposition of perovskites into PbI_2 and either FAI or MAI that can be easily evaporated.[9] This phenomenon can be further accelerated under thermal conditions. To avoid such degradation in OIHPs, numerous efforts have been attempted. For instance, hydrophobic materials such as $C_6H_5(CH_2)_2NH_3^+$ (phenylethylammonium, PEA^+) and $CH_3(CH_2)_3NH_3^+$ (butylammonium, BA^+) are added to 3D OIHPs to form more bulky quasi- 2D structures to protect the perovskite layer.[10] The hydrophobic organic spacer that acts as a moisture barrier in quasi-2D perovskites has shown to provide a better ambient stability with decent device performances, immobilizing ion species as compare to the 3D perovskite counterparts.[11−13] However, the photovoltaic performance of devices with quasi-2D perovskites still lags behind that of 3D perovskites as the incorporation of a large cation leads to lower charge carrier concentration,[14] higher exciton binding energy,[15] and anisotropic charge carrier transport.[16] Thus, it is important to understand the mechanisms behind charge carrier dynamics in quasi-2D perovskites for further development of devices with higher ambient stability.

It was first reported that the PEA incorporation into $MAPbI_3$ forms $(PEA)_2(MA)_2Pb_3I_{10}$ layered perovskite, possessing a power conversion efficiency (PCE) of 4.74% in solar cells and higher stability under humid condition.[17] PEA^+ self-assembles with the inorganic sheet that is typically lead halide octahedral, exceeding the tolerance space of the 3D framework.[18] With a

Received: April 28, 2021
Accepted: June 29, 2021

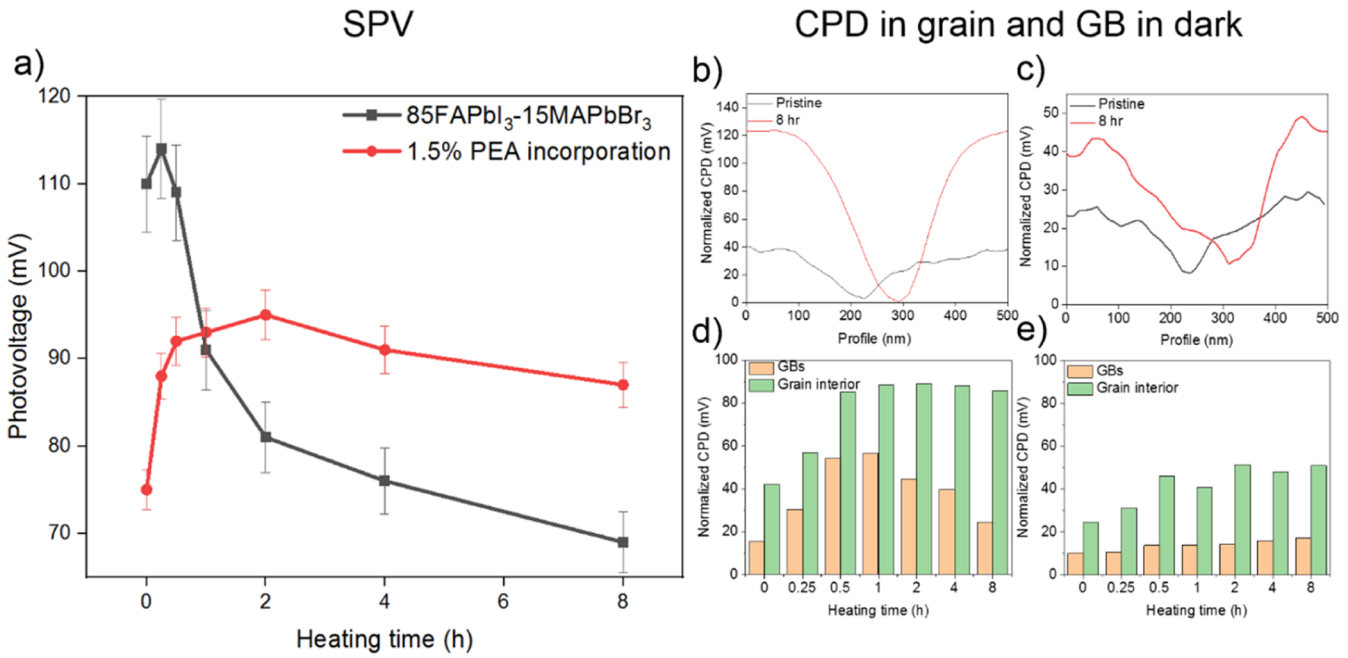

Figure 1. Thermal and humidity stability in double-cation and double-halide (3D) $85FAPbI_3$-$15MAPbBr_3$ perovskites and quasi-2D perovskite counterparts. (a) Photovoltage variations as a function of heating time in ambient air in the two films. The CPD profile at GBs in the pristine state (black) and after heating the film at 50 °C for 8 h (red) in ambient air in (b) 3D films and (c) quasi-2D films. Averaged CPD in 10 grain interiors and GBs as a function of heating time in ambient air in (d) 3D perovskite and (e) quasi-2D perovskite films.

strong interlocking force between the organic and inorganic species, 2D structures have led to better ambient stability.[19] Later, the PEA incorporation into $FAPbI_3$ resulted in a relatively satisfying solar cell performance with a PCE of 17.7% and ambient stability due to passivating defects at GBs.[20] Further, optimizing the amount of PEA cations in double-cation and double-anion perovskites resulted in highly improved moisture stability of solar cells and PCE of 17.1%.[21] Meanwhile, the thermal stability has been improved via direct growth of 2D $(PEA)_2PbI_4$ on top of the 3D perovskite film where the ultrathin $(PEA)_2PbI_4$ layer provides better band energy alignment and protecting the 3D perovskite layer, resulting in solar cells with PCE of around 20.7%.[22] As discussed earlier, when the quasi-2D perovskite is solely used as an absorber layer, the corresponding solar cell is likely to have a relatively low PCE. However, the underlying reasons behind the low efficiency of quasi-2D perovskite solar cells are still unclear.

Here, we synthesize quasi-2D perovskites by incorporating the PEA cation into double-cation and double-halide $85FAPbI_3$-$15MAPbBr_3$ perovskites deposited on the SnO_2/indium tin oxide (ITO) glass substrate. We confirm a PEA-incorporated quasi-2D perovskite via X-ray diffraction (XRD) and Kelvin probe force microscopy (KPFM) measurements. KPFM results reveal that GB passivation in quasi-2D perovskites contributes to the slow degradation in ambient air at 50 °C. We further explore the spatial distribution of photoconductivity in both 3D and quasi-2D films using bias-dependent conductive atomic force microscopy (c-AFM). Local $I-V$ characteristics are also explored utilizing a c-AFM setup. To investigate interfacial charge carrier dynamics, Au electrodes are laterally deposited on the thin films. We apply a first-order reversal curve (FORC) electric bias waveform that contains gradually increasing and decreasing pulsed biases with on- and off-fields to the electrodes to inject and release charge carriers. Using FORC electric bias, we explore time-resolved contact potential difference (CPD) and current variations in dark and under illumination in the lateral devices. Our results reveal higher CPD variation at the interface and two times higher current in the 3D perovskite-based device as compared to the quasi-2D counterparts. Our study provides an important insight for further improvement of efficiency and stability in designing perovskite-based devices.

RESULTS AND DISCUSSION

We fabricate double cation and double halide $85FAPbI_3$-$15MAPbBr_3$ 3D perovskite films on the SnO_2/ITO glass substrate. This is a highly efficient and stable perovskite composition optimized by compositional engineering for solar cells.[4] To synthesize quasi-2D perovskites, we incorporate phenylethylammonium (PEA) into the $85FAPbI_3$-$15MAPbBr_3$ perovskite. Details of the fabrication procedure can be found in the Experimental Section. As a model system, we choose PEA 1.5 mol %-incorporated $85FAPbI_3$-$15MAPbBr_3$ perovskites using the $PEAPbI_3$ precursor. This ratio was previously demonstrated by Lee et al.[21] with relatively higher efficiency and superior stability under 70% relative humidity (RH) than other mixing ratios, for example, 3.0, 4.5, and 10 mol %. Notably, a higher concentration of large molecular cations leads to a higher band gap and low charge carrier concentrations.[23] Typically, double-cation and double-halide perovskites have an intrinsically nonuniform distribution of chemical composition within the film.[24] Thus, when PEA is mixed with both $FAPbI_3$ and $MAPbBr_3$, it can result in multiple n-values within the film[21] as compared to PEA incorporation into a single-organic cation perovskite such as $MAPbI_3$. When PEA is incorporated into the $MAPbI_3$ perovskite, that is, $(PEA)_2(MA)_{n-1}PbI_{3n+1}$,[25] the n-value is tuned by the PEA concentration. In a quasi-2D perovskite, the n-value defines the thickness of the 2D layer and controls optical and electrical properties. Although the n-value can be theoretically controlled by modulating the stoichiometric ratio of organic cations in precursor solution, practically it is

https://doi.org/10.1021/acsami.1c07876
ACS Appl. Mater. Interfaces XXXX, XXX, XXX−XXX

difficult to obtain a single *n*-value during synthesis, especially via solution processes.[26−28] Therefore, we do not consider controlling the *n*-value in our study.

To characterize the PEA-incorporated 85FAPbI$_3$-15MAPbBr$_3$ perovskites, XRD measurements are carried out, as shown in Figure S1. The characteristic 85FAPbI$_3$-15MAPbBr$_3$ perovskite peaks of (110), (200), (202), (220), and (222) planes are indexed at 14, 19.9, 24.4, 28.3, and 31.8°,respectively, similar to the previous report.[21] When PEA is incorporated, the intensities of (110) and (220) planes are noticeably increased. It was previously observed that intensity of the (110) peak increases as the PEA concentration in the 85FAPbI$_3$-15MAPbBr$_3$ perovskite increases due to enhancement of crystallinity.[21]

To compare the ambient stability of 85FAPbI$_3$-15MAPbBr$_3$ thin films with and without PEA incorporation, the KPFM measurements were performed immediately after the films were heated on a hot plate (50 °C) in ambient air (RH ∼ 40%). To find the same regions for the measurements, we marked the film surface with a blade. Note that the KPFM measurements in dark are carried out when the microscope light is turned off after finding the location on the film, while the measurements under light conditions are carried out when a commercial LED light source illuminated the sample from the bottom through the glass substrate. Once the measurements were completed, the samples were moved to the hot plate again for longer heating. The KPFM technique allows for simultaneous imaging of the topography and spatial CPD, providing information of surface potentials, surface photovoltage, charge carrier dynamics, and the internal electric field.[29−31] Figure 1a shows the time evolution of surface photovoltage (SPV) in both films at 50 °C in ambient air. The SPV is obtained from subtraction of $CPD_{light} - CPD_{dark}$ after normalizing CPD, indicating that the perovskite absorber operates between dark and illumination. The full series of CPD maps are shown in Figures S2 and S3. To measure the SPV, the line profiles under each condition are plotted in Figure S4, showing significant increase in the CPDs. Then, the SPV is plotted as a function of heating time as shown in Figure 1a. The initial photovoltage is larger in the 3D perovskite film (see Figure 1a) but it exponentially decreases by 70% when the film is kept at 50 °C for 2 h and then continuously drops to around 60% after 8 h. In contrast, although a relatively small SPV is initially observed in the quasi-2D film, the SPV increases by 25% at 50 °C for 2 h and then it gradually decreases to approximately 8% after 8 h. It was previously reported that a mild moisture-induced grain growth can be beneficial for charge carrier transport.[32] To explore this phenomenon, we compare the topography images (Figure S5a,b) between the fresh and heated films and extract the average grain sizes (Figure S5c). The topography images and analysis of the grain size before and after 2 h heating reveal an initial grain growth between the two conditions. This observation is consistent with the previous study.[32] Note that the SPV in the early stage (before 1 h) is higher in the 3D perovskite than in the quasi-2D perovskite thin films. Despite mild moisture conditions (RH ∼ 40%), the significant reaction with the 3D perovskite film results in fast degradation. These results indicate that PEA-incorporated films are more ambient and thermally stable than the films without PEA. We notice a transient behavior in the CPD profile at the bottom edge in Figures S2 and S3 when the film is under the dark condition. The higher CPD at the bottom edge of the images can be resulted from the relaxation of residual photoexcited charge carriers when the microscope light was initially used to find out the locations on the film surface. Note that the microscope light has a lower intensity than the LED source used for illuminating the samples. Thus, the CPD gradient at the bottom edge in the images could be an indication of the extent of the charge relaxation, the so-called transient behavior. Such a transient behavior is dependent on the duration of heating in both films as shown in Figure S4. The transient behavior is less in the pristine state (before heating) while it increases as the heating time is prolonged. Therefore, the transient behavior results from residual photocurrent, which is also influenced by prolonged heating and exposure to the humid conditions.

We further explore the CPD variations between grain interior and the GBs to study degradation. Figure 1b,c shows line profiles between grain interior and GBs before and after exposure to heat and humidity for 8 h in both films. The individual CPD maps in dark are displayed in Figure S6. The line profiles in Figure 1b,c are obtained from blue and red lines in Figure S6. All CPD values at GBs are normalized for direct comparison between each condition. Originally, the CPD values at GBs are reduced after heating the samples for 8 h as shown in Figure S7. However, without normalizing the values, it is difficult to compare CPDs between the two conditions due to significant difference; thus the normalized CPDs are plotted in Figure 1b,c. As can be seen in Figure 1b, in the 3D perovskite films, the CPD gap between grain and GB is relatively small, ∼40 mV, while the gap significantly increases to ∼120 mV after exposure to thermal and humid conditions for 8 h. It is known that the degradation initiates at the GBs when humidity is introduced. It was computed via Car−Parrinello molecular dynamics that moisture contributes to the release of mobile I^- ions due to interaction between water and Pb^{2+} ions in $MAPbI_3$ perovskites.[33] Previous experimental results show that the increasing CPD gap between grain interior and GBs is indicative of degradation of the film due to moisture penetration.[8] Thus, our results confirm that moisture severely penetrates along the GBs in the 3D perovskites under thermal and humid conditions. However, the observed initial CPD gap in the quasi-2D perovskite is relatively smaller, ∼10 mV, and it experiences a small increase up to around 30 mV under the same conditions. These results indicate that quasi-2D perovskites degrade very slowly compared to the 3D perovskite counterparts. To further analyze this effect, we selected 10 more grains and GBs for statistical analysis and the averaged values are plotted in Figure 1d,e. It is noticeable that the CPD gaps are quickly increased as a function of heating time in ambient air in 3D perovskites whereas they are slowly increased in quasi-2D perovskites. Our results confirm that the PEA successfully passivates defects, especially at the GBs.

To gain insight into the conduction behavior, nanoscale photocurrents are mapped using c-AFM by applying a positive bias of +0.3 V to the sample. Note that this applied bias is optimized to visualize a clear photocurrent map without noise. When higher biases above +0.5 V are applied, we observe significant noises during scanning due to serious ion migration. In this case, mobile organic cations vigorously migrate to the top surface, interrupting the collection of the photocurrent. Note that a positive bias attracts negative ions such as I^- and Br^- to the bottom region of the perovskite layer and repels positive ions such as FA^+, MA^+, and Pb^{2+} to the film surface and vice versa for negative bias. The simple illustration of this measurement is described in Figure S8. The characterization of the ion migration behavior using AFM has been previously demonstrated by us[30,34] and Yun et al.[29] in OIHPs. Particularly, the application of

https://doi.org/10.1021/acsami.1c07876
ACS Appl. Mater. Interfaces XXXX, XXX, XXX−XXX

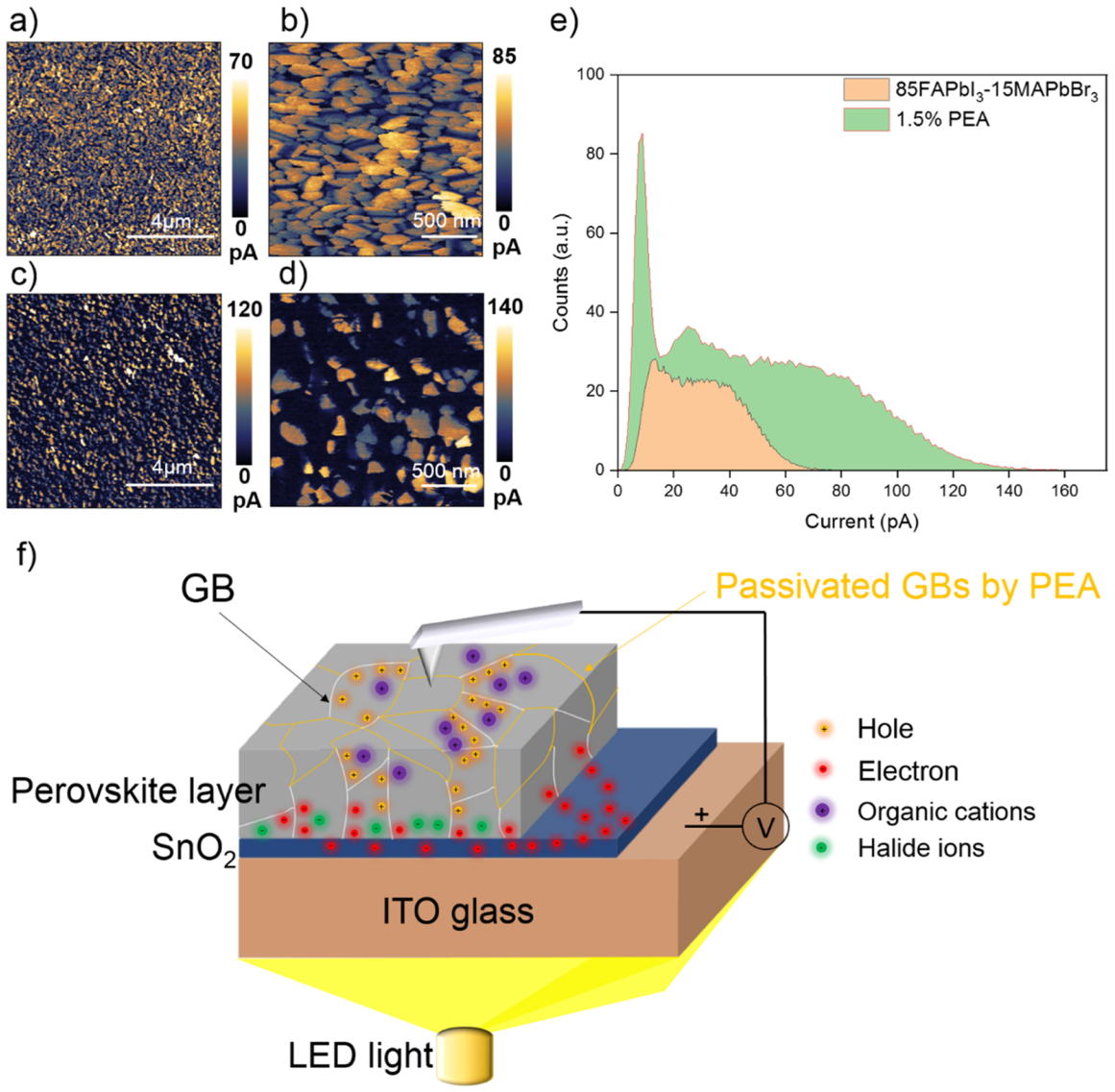

Figure 2. Surface conductivity in 3D and quasi-2D perovskites measured by light-assisted c-AFM. Local photocurrent map over an area of (a) 100 and (b) 4 μm^2 under illumination and +0.3 V bias in a 3D perovskite and (c,d) quasi-2D perovskite. (e) Histogram plot of the c-AFM scan data in (a,c) where *x*-axis represents current and *y*-axis represents the frequency of data points. (f) Schematic illustration of charge separation and selective accumulation of holes in specific grains in the quasi-2D perovskite due to GB passivation.

higher biases (>− 4 V) to the AFM tip allows positive ions to severely move to the top surface, which can cause irreversible damages due to escaping mobile organic cations on the film surface.[29,34] Thus, we carefully apply a small bias (+0.3 V) to the ITO conductive substrate to produce clear photocurrent maps without noise and to avoid the surface damage.

Figure 2a,b shows photocurrent maps of the 3D perovskite where the sample is illuminated through the glass substrate using a commercial white LED source. There are relatively uniform currents in individual grains in both maps. However, strong grain-by-grain variability is observed in the quasi-2D perovskite as shown in Figure 2c,d. This inhomogeneous conduction behavior can be associated with GB passivation. Blocking the pathways for charge carrier transport, for example, GBs, leads to grain-by-grain inhomogeneous conductivity in the quasi-2D perovskite where higher conductivity is preferentially along the specific grains. The poor efficiency of the quasi-2D perovskite was previously associated with the energy transfer processes[28] from high-band gap quasi-2D or 2D perovskites (lower n value) to the low-band gap 3D perovskites. This phenomenon was measured via time-resolved photoluminescence decays and transient absorption spectroscopy on picosecond time scale.[35] Here, the timescale for c-AFM measurements is a few minutes up to 10 min. Although we do not rule out the energy transfer effect, our collective results with similar timescales confirm that the non-uniform conductivity could be one of the possible reasons for the lower density of charge carriers and poor efficiency of quasi-2D perovskites. The corresponding topography maps of samples in Figure 2a−d are displayed in Figure S9. Interestingly, a morphological change is observed between the two thin films. The grain sizes in the PEA quasi-2D perovskite films are slightly larger ∼300−400 nm as compared to ∼200−300 nm in the 3D perovskite counterpart. It is well established that the increase in grain size and decrease in GBs is essential for highly efficient perovskite solar cells.[36] The increased grain size is due to stronger interaction between PEA^+ and Pb^{2+} ions, correlating with the Ostwald-type ripening mechanism[37] where higher surface energies induce crystal

https://doi.org/10.1021/acsami.1c07876
ACS Appl. Mater. Interfaces XXXX, XXX, XXX−XXX

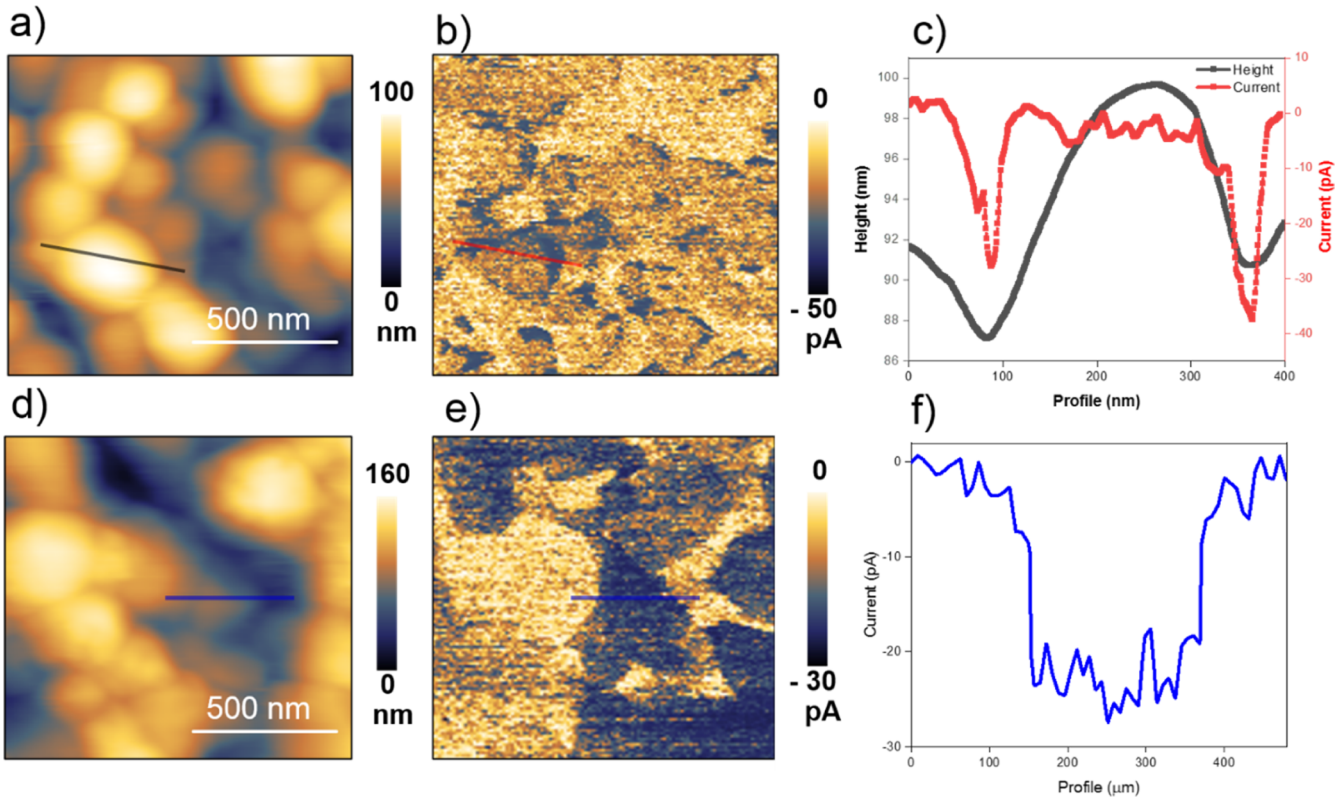

Figure 3. Surface conductivity of 3D and quasi-2D perovskites using c-AFM measurements when a negative bias is applied to the ITO conductive substrate. (a) Topography image, (b) spatial photocurrent map under illumination with −3 V bias, and (c) line profile of the marked line in (b) 3D perovskites and (d−f) quasi-2D perovskites.

growth. To further analyze the distribution of current, we explore the histogram plot in Figure 2e, which is obtained from Figure 2a,c. Although a higher total current is observed in quasi-2D perovskites than 3D perovskites, the inhomogeneity in the current distribution is noticeable in the quasi-2D perovskites. As discussed earlier, this inhomogeneous conduction can be possibly due to GB passivation as GBs can play a beneficial role in charge transport.[38]

To obtain an insight into charge carrier dynamics, we construct local $I-V$ curves with higher biases and different sweeping rates (see Figure S10) to study the hysteretic behavior in thin films. It is interesting to note that the resultant $I-V$ curves show relatively small hysteresis in 3D perovskites, while the observed hysteretic currents in quasi-2D perovskites are significantly larger. This hysteretic behavior is sweep-rate-dependent (Figure S10b). Particularly, when the sweep rate is increased up to 1 Hz (256 steps per sec, around 7.8 s), the hysteretic behavior significantly increases. Similar local hysteretic behaviors are recently observed in the quasi-2D $(PEA)_2Cs_3Pb_4I_{13}$ perovskite.[39] Due to the wider band gap of quasi-2D perovskites, they form a higher Schottky barrier, leading to resistive switching dynamics.[39] Typically, the Schottky barrier is formed at the interface between semiconductor and metal electrodes, owing to the work function difference.[40] Another possible mechanism for this hysteretic behavior can be associated with some grains covered with the insulating hydrophobic PEAI. The schematic of such a mechanism is shown in Figure 2f. Due to insulation of some grains by GB passivation, the charge carriers are selectively accumulated in specific grains that are not passivated and can be a selective pathway for charge transport. Thus, it is expected that the ionic charge carriers nonuniformly migrate to specific grains. Consequently, larger local $I-V$ hysteresis is observed in quasi-2D perovskites as compared to the 3D perovskite counterpart.

Next, we investigate the surface conductivity of the thin films by applying a negative bias to the ITO conductive substrate. Upon application of negative biases, the polarity of the current changes from positive to negative values where the electron charge carriers are dominated on the film surface. In this case, the halide ions and electron charge carriers move to the top surface due to the repulsive force, generating a negative current.

Figure 3a,b shows topography and photocurrent maps at −3 V in 3D perovskites. The line profile of the current in Figure 3b is displayed in Figure 3c. As can be seen, there are two sharp currents at GBs. It is well-documented that GBs play a major role in the optoelectronic properties of OIHPs.[41−43] Using solution processes, GBs are inevitable in polycrystalline films. Although these GBs are pathways for the charge carrier transport,[29,38] the structural disorder at GBs forms defect states which can potentially degrade optoelectronic properties.[8] These results further confirm that charge carriers are collected at GBs in 3D perovskites. In contrast, such behavior is not observed in quasi-2D perovskites as shown in Figure 3d−f. In this case, the currents appear not at the GBs but in some grain interiors. This result confirms that some grains and GBs are partially passivated by PEA incorporation, resulting in smaller currents. Despite higher stability by GB passivation in quasi-2D perovskites, the reduced electronic and ionic charge carrier transport can be potentially detrimental to the globally efficient charge collection.

We do not observe noise during c-AFM scans when a negative bias is applied. We have previously shown that organic cations, for example, FA^+ and MA^+, can dissociate on the top surface,

https://doi.org/10.1021/acsami.1c07876
ACS Appl. Mater. Interfaces XXXX, XXX, XXX−XXX

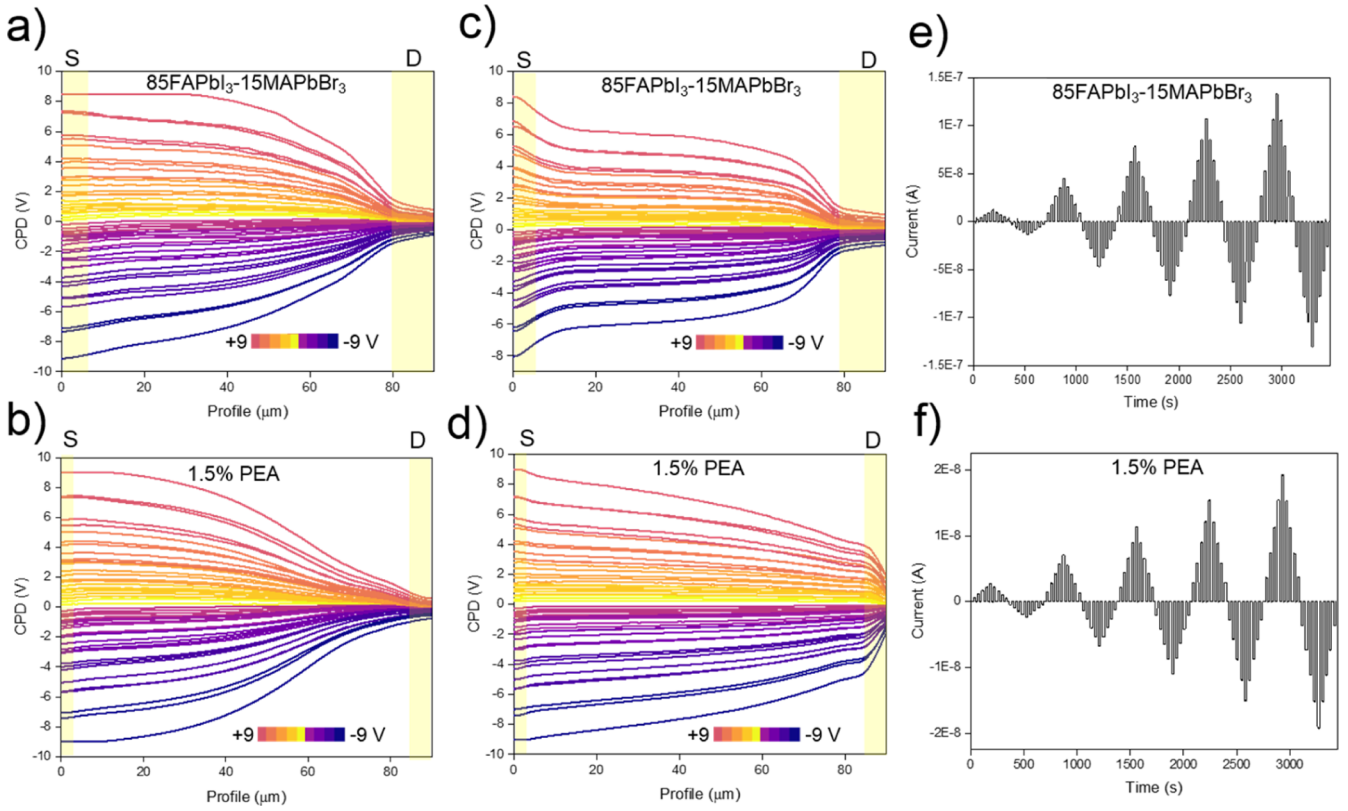

Figure 4. Charge transport in the lateral 3D and quasi-2D perovskites devices, utilizing FORC bias driven-KPFM and $I-V$ measurements. CPD variation across perovskites between source and drain electrodes in (a) 3D and (b) quasi-2D perovskites devices in dark and (c,d) under illumination. The $I-t$ (current−time) curve in (e) 3D and (f) quasi-2D perovskites devices under illumination.

forming a hump at GBs when a higher bias is applied to the AFM tip (>−7 V) while halide anions, for example, I^- and Br^-, do not damage the film even under higher biases (>+7 V).[34] In this measurement, applying a negative bias to the ITO substrate is analogous to applying a positive bias to the AFM tip. This means that charge carriers move in the opposite direction by applying the bias to either the ITO substrate or AFM tip. Hence, we can explore the negative bias-dependent conduction behavior in the thin films without significant noise as shown in Figure S11. Interestingly, the current is collected at GBs at −3 V, and it flows to the interior grains at −4 V in 3D perovskites (see Figure S11a−d). However, the current can be observed only at some GBs. It was recently reported that there are two types of GBs: (1) charge carrier pathways and (2) limited vertical conduction.[44] Therefore, here the observation of conductivity at some GBs are consistent with the previous study. As can be seen in Figure S11e−h, the quasi-2D perovskites show a different conduction behavior with higher current in some grains and lower in others. Contrary to 3D perovskites, we cannot observe noticeable current at GBs in the quasi-2D perovskite. These results suggest that GBs are passivated in quasi-2D perovskites, revealing no charge carrier collection at GBs. Interestingly, some stripe-patterned conduction is observed in the grains at −4 V (red circles in Figure S11h). Such stripe-patterned conduction along with topographical corrugations (Figure S12) can be associated with ferroelastic domains that stem from internal strains during the annealing process.[45] The ferroelastic domains were previously observed under illumination and electrical biases in some grains in the 3D $85FAPbI_3$-$15MAPbBr_3$ perovskites.[34] This is due to the inhomogeneous distribution of internal strains induced by chemical gradients in the films.[46]

The correlation between domain structures and charge transport in quasi-2D perovskites is not clear yet and will be the subject of future studies. The measured sharp current at the GBs in 3D perovskites (see Figure 3c) is around two times higher than the current in grains in quasi-2D perovskites (see Figure 3f). It was reported that GBs in OIHPs do not produce deep energy states, unlike classical Si polycrystalline films.[38] Instead, the GBs are electrically charged, generating built-in potential, which plays an important role in efficient charge separation. Thus, photocurrent can be enhanced at GBs. We expect this local conduction behavior can affect the global charge dynamics in devices, which is discussed in the following section.

To further investigate charge carrier properties, we utilize the FORC electrical bias waveform during KPFM and $I-V$ measurements on the Au electrode-deposited lateral devices. Note that the FORC waveform contains on- and off-fields where each bias step takes 19 s. The on-field biases include gradually increasing and decreasing steps from 0 to +1, −1, +3, −3, +5, −5, +7, −7, +9, and −9 V. The time-resolved KPFM technique with the FORC waveform is recently used for the OIHP lateral devices to explore electronic/ionic charge carrier dynamics.[47] This is a common technique to obtain the electronic/ionic charge carrier and electric field distribution by measuring surface potential variations. When the variable biases are applied to the source electrode, spatial CPD variation provides information regarding the surface electric field and charge carrier distribution.

Figure 4a,b shows spatial CPD distributions between the source and drain electrodes across the perovskite channel as a function of bias in 3D and quasi-2D perovskites under dark conditions. The injected charge carriers that are generated from

https://doi.org/10.1021/acsami.1c07876
ACS Appl. Mater. Interfaces XXXX, XXX, XXX−XXX

the source electrode and charges formed in the perovskite layer move to the drain electrode, leading to potential drops around the drain electrode. Sharper potential drops can be observed at the 3D perovskite-drain interface. On the other hand, the potential distributions are significantly different in quasi-2D perovskites (Figure 4b,d) and the potential drops slowly in the perovskite-drain regions. This result indicates that the generated charge carriers are quantitatively lower in the quasi-2D perovskites than 3D perovskites. Similarly, the potential distributions are explored under illumination as shown in Figure 4c,d. The potential drops are strikingly visible at the source interface and much higher drops are observed at the perovskite-drain interface in both samples as compared to dark conditions. Similarly, more potentials drops are shown in 3D perovskites under illumination (Figure 4c). Further, the electric field distribution and charge carrier concentrations were estimated under +7 V bias by calculating the first and second derivatives of CPD, respectively (Figure S13). The temporal dynamic of the electric field is similar for both samples in dark despite higher electric fields around the drain electrode in 3D perovskites (see Figure S13a). As expected, charge carrier concentrations in 3D perovskites are slightly higher at both electrode interfaces (Figure S13b). However, in the quasi-2D perovskite, such difference significantly increases in the source electrode and perovskite regions under illumination (Figure S13c,d) although the carrier concentration is slightly higher at the drain electrode. This result shows relatively lower charge carriers in the quasi-2D perovskite, which is consistent with inhomogeneous conductivity and lower negative current in c-AFM results. Finally, we explore FORC-driven $I-V$ characteristics of the lateral devices. The current dynamics under dark conditions are displayed in Figure S14. The measured currents in 3D perovskites are two times higher than quasi-2D perovskites as shown in Figure S14a,b. To further investigate the transient dynamics, we separately plot the currents during on- and off-fields (Figure S14c–f). The current dynamics are linear under the on-field conditions as a function of bias while hysteretic dynamics are observed in quasi-2D perovskites during the off-fields (see Figure S14f). This hysteretic behavior is associated with ion migration and accumulation at the interfaces. The observed hysteresis in quasi-2D perovskites during off-fields suggests the slow dynamic of ions. The suppression of ion migration and GB passivation in quasi-2D perovskites were demonstrated in previous sections. Therefore, it can be concluded that ions are not freely movable in quasi-2D perovskites due to locking by the GB passivation, but ions can still migrate grain-by-grain. These migrated ions accumulate at some defective sites during on-fields and slowly relax under off-field conditions. We also observe one order of magnitude higher current in 3D perovskites than quasi-2D counterparts under illumination. Both samples show less transient behavior under illumination (Figure 4e,f) than in dark. The reduced transient dynamics are due to faster charge motions, originating from higher density of photogenerated charge carriers.

A non-uniform conductivity and lower charge carrier concentration in quasi-2D perovskites than in 3D perovskite counterparts were demonstrated using c-AFM, KPFM, and $I-V$ measurements. Despite better ambient stability of quasi-2D perovskites, relatively lower charge carrier concentrations could contribute to lower PCE in quasi-2D based-solar cells. For example, as PEA incorporation increases, current density in solar cell devices decreases.[21] Our results explain the mechanism behind lower current density in PEA-incorporated perovskite solar cells.

CONCLUSIONS

In summary, we have successfully incorporated PEA into double-cation and double-halide 85$FAPbI_3$-15$MAPbBr_3$ perovskites. The KPFM measurements demonstrate that the PEA-incorporated perovskite, namely, the quasi-2D perovskite, has better thermal and ambient stability due to passivating GBs. The light-assisted KPFM measurements show that in quasi-2D perovskites, the photovoltage slowly decreases after 8 h at 50 °C despite overall lower photovoltage, while the photovoltage degrades fast in 3D perovskite counterparts. The photocurrent maps obtained by light-assisted c-AFM reveal that the photocurrent is higher in quasi-2D perovskites with inhomogeneous conductivity from grain-to-grain. However, a relatively uniform conduction behavior is observed in individual grains of the 3D perovskites despite lower conduction. The photocurrent maps under negative biases exhibit higher conduction at GBs in the 3D perovskites and lower conduction in grain interior in the quasi-2D perovskites. The charge carrier dynamics studied via FORC $I-V$ and CPD variations are significantly different between the two devices. The higher electric field and charge carrier distributions observed in 3D perovskites are due to higher ionic conductions, whereas in the quasi-2D perovskites, hysteretic behaviors under off-field conditions is observed in $I-V$ curves under dark conditions, owing to slow dynamic of ions. This result is consistent with local $I-V$ hysteresis in the c-AFM measurement. This study elucidates the underlying mechanisms for local and global conduction behaviors in quasi-2D and 3D perovskites and provides a pathway for further development of perovskite-based devices.

EXPERIMENTAL SECTION

Perovskite Film Synthesis. All chemicals used here were purchased from Sigma-Aldrich and used without any further purifications. The $(FAPbI_3)_{0.85}(MAPbBr_3)_{0.15}$ precursor solution was prepared by dissolving 1.38 M FAI and PbI_2 and 1.38 M MABr and $PbBr_3$ in *N*,*N*-dimethyl formamide (DMF, 99.9%)/dimethyl sulfoxide (DMSO, 99.7%) mixed solvent (4:1 volume ratio). The prepared $FAPbI_3$ and $MAPbBr_3$ precursor solutions were stirred at 60 °C for 1 h and then mixed for the desired $(FAPbI_3)_{0.85}(MAPbBr_3)_{0.15}$ composition. PEAI and PbI_2 were dissolved in DMF and DMSO mixed solvent with the same ratio. The prepared $PEAPbI_3$ precursor solutions were stirred at 60 °C for 1 h and then added in the $(FAPbI_3)_{0.85}(MAPbBr_3)_{0.15}$ precursor solution at 1.5%:100% ratio. The ITO glass substrates (MSE Pro, 15 × 15 × 1 mm^3) were precleaned using deionized water, acetone, and isopropanol in an ultrasonic bath for 15 min, respectively. After cleaning processes, the glass substrates were treated under UV ozone for 15 min. For electron transport layer deposition, the diluted SnO_2 precursors (6.7%) with DI water were spun at 3000 rpm for 30 s on the precleaned ITO glass substrate. Then, the films were dried on a hot plate at 100 °C for 10 min. The substrates were transferred to an N_2-filled glovebox. The $(FAPbI_3)_{0.85}(MAPbBr_3)_{0.15}$ and 1.5%PEA-incorporated $(FAPbI_3)_{0.85}(MAPbBr_3)_{0.15}$ solutions were spun at 2000 and 6000 rpm for 10 and 25 s, respectively. The anti-solvent chlorobenzene was drop-casted (150 μL) during the last 15 s of spin coating. All films were immediately annealed at 100 °C for 10 min.

Characterizations. *XRD Measurements.* The crystal structure and crystal orientation of the films were characterized using a high-resolution X-ray diffractometer (X'Pert Pro, Panalytical) using Cu Kα radiation.

Scanning Probe Microscopy (SPM) Measurements: KPFM and c-AFM. The thin films were characterized by AFM (MFP-3D, Asylum Research) under ambient condition at room temperature. All

https://doi.org/10.1021/acsami.1c07876
ACS Appl. Mater. Interfaces XXXX, XXX, XXX−XXX

SPM measurements were performed using a Pt-/Ir-coated Si cantilever (ElectriMulti 75-G, Budget Sensors). For KPFM, a lift height of 50 nm was used to detect optimized contact potential difference. For c-AFM, a dual-gain ORCA (Asylum Research) cantilever holder possessing a current range of 1 pA to 10 μA was used to measure local photocurrent maps and $I-V$ characteristics. A white LED source without any filter was used to illuminate the sample through the glass substrate. A contact wire was mounted on the back of the cantilever holder and attached to the ITO substrate to build a close circuit between the tip and ITO substrate. In all SPM measurements, the scan rate was fixed at 1.0 Hz and the scan direction started from top to bottom of the image.

KPFM and *I*–*V* Measurements in the Lateral Device. *Lateral Device Fabrication.* The $(FAPbI_3)_{0.85}(MAPbBr_3)_{0.15}$ and 1.5% PEA-incorporated $(FAPbI_3)_{0.85}(MAPbBr_3)_{0.15}$ solutions were deposited on the precleaned glass substrates (MSE Pro, 15 × 15 × 1 mm^3). The 50 nm-thick Au electrodes were deposited by thermal evaporation using a shadow mask with a channel distance of around 70 μm.

FORC Biases with On- and Off-Field on the Lateral Device. The FORC waveform electrical biases with on- and off-fields were applied to the lateral devices during KPFM measurements. The $I-V$ measurements are simultaneously carried out during KPFM scans. The electrical biases were supplied using a Keithley 2450 source meter controlled using a test script builder. After applying biases in the dark and then relaxation for 40 min in dark, the photo-induced CPD distribution between electrodes across the perovskite layer was measured under illumination.

■ ASSOCIATED CONTENT

Supporting Information

The Supporting Information is available free of charge at https://pubs.acs.org/doi/10.1021/acsami.1c07876.

XRD patterns of the thin films, normalized CPD spatial maps in dark and under illumination, line profile analysis, topography maps and average grain size plots, normalized CPD spatial maps in dark, raw data of CPD maps and line profiles, c-AFM setup, topography images corresponding to c-AFM current maps, sweep-rate-dependent local $I-V$ characteristics, bias-dependent current maps, height profile from topography image, 1st and 2nd derivates of the CPD line profile of the lateral devices, and FORC-driven current–time ($I-t$) curves and current–voltage ($I-V$) curves in dark and under illumination (PDF)

■ AUTHOR INFORMATION

Corresponding Authors

Dohyung Kim – *Department of Materials Science and Engineering, University of Tennessee, Knoxville, Tennessee 37996, United States;* orcid.org/0000-0002-1586-1466; Email: dkim48@utk.edu

Mahshid Ahmadi – *Department of Materials Science and Engineering, University of Tennessee, Knoxville, Tennessee 37996, United States;* orcid.org/0000-0002-3268-7957; Email: mahmadi3@utk.edu

Complete contact information is available at: https://pubs.acs.org/10.1021/acsami.1c07876

Notes

The authors declare no competing financial interest.

■ ACKNOWLEDGMENTS

M.A. acknowledges support from the National Science Foundation (NSF), Award Number # 2043205. M.A. and D.K. acknowledge support from the University of Tennessee StART-alliance project. XRD was performed at the Joint Institute for Advanced Materials (JIAM) Diffraction Facility, located at the University of Tennessee, Knoxville.

■ REFERENCES

(1) Huang, J.; Yuan, Y.; Shao, Y.; Yan, Y. Understanding the Physical Properties of Hybrid Perovskites for Photovoltaic Applications. *Nat. Rev. Mater.* **2017**, *2*, 17042.

(2) Ahmadi, M.; Wu, T.; Hu, B. A Review on Organic–Inorganic Halide Perovskite Photodetectors: Device Engineering and Fundamental Physics. *Adv. Mater.* **2017**, *29*, 1605242.

(3) Sutherland, B. R.; Sargent, E. H. Perovskite Photonic Sources. *Nat. Photonics* **2016**, *10*, 295–302.

(4) Jeon, N. J.; Noh, J. H.; Yang, W. S.; Kim, Y. C.; Ryu, S.; Seo, J.; Seok, S. I. Compositional Engineering of Perovskite Materials for High-Performance Solar Cells. *Nature* **2015**, *517*, 476–480.

(5) Jung, E. H.; Jeon, N. J.; Park, E. Y.; Moon, C. S.; Shin, T. J.; Yang, T.-Y.; Noh, J. H.; Seo, J. Efficient, Stable and Scalable Perovskite Solar Cells using Poly(3-hexylthiophene). *Nature* **2019**, *567*, 511–515.

(6) Yoo, J. J.; Seo, G.; Chua, M. R.; Park, T. G.; Lu, Y.; Rotermund, F.; Kim, Y.-K.; Moon, C. S.; Jeon, N. J.; Correa-Baena, J.-P.; Bulović, V.; Shin, S. S.; Bawendi, M. G.; Seo, J. Efficient Perovskite Solar Cells via Improved Carrier Management. *Nature* **2021**, *590*, 587–593.

(7) Wang, Q.; Chen, B.; Liu, Y.; Deng, Y.; Bai, Y.; Dong, Q.; Huang, J. Scaling Behavior of Moisture-Induced Grain Degradation in Polycrystalline Hybrid Perovskite Thin Films. *Energy Environ. Sci.* **2017**, *10*, 516–522.

(8) Yun, J. S.; Kim, J.; Young, T.; Patterson, R. J.; Kim, D.; Seidel, J.; Lim, S.; Green, M. A.; Huang, S.; Ho-Baillie, A. Humidity-Induced Degradation via Grain Boundaries of $HC(NH_2)_2PbI_3$ Planar Perovskite Solar Cells. *Adv. Funct. Mater.* **2018**, *28*, 1705363.

(9) Berhe, T. A.; Su, W.-N.; Chen, C.-H.; Pan, C.-J.; Cheng, J.-H.; Chen, H.-M.; Tsai, M.-C.; Chen, L.-Y.; Dubale, A. A.; Hwang, B.-J. Organometal Halide Perovskite Solar Cells: Degradation and Stability. *Energy Environ. Sci.* **2016**, *9*, 323–356.

(10) Jung, M.-H. Hydrophobic Perovskites Based on an Alkylamine Compound for High Efficiency Solar Cells with Improved Environmental Stability. *J. Mater. Chem. A* **2019**, *7*, 14689–14704.

(11) Xie, Y.; Yu, H.; Duan, J.; Xu, L.; Hu, B. Enhancing Device Performance in Quasi-2D Perovskite ($(BA)_2(MA)_3Pb_4I_{13}$) Solar Cells Using PbCl2 Additives. *ACS Appl. Mater. Interfaces* **2020**, *12*, 11190–11196.

(12) Wang, F.; Wang, Z.; Sun, W.; Wang, Z.; Bai, Y.; Hayat, T.; Alsaedi, A.; Tan, Z. a. High Performance Quasi-2D Perovskite Sky-Blue Light-Emitting Diodes Using a Dual-Ligand Strategy. *Small* **2020**, *16*, 2002940.

(13) Fu, W.; Wang, J.; Zuo, L.; Gao, K.; Liu, F.; Ginger, D. S.; Jen, A. K. Y. Two-Dimensional Perovskite Solar Cells with 14.1% Power Conversion Efficiency and 0.68% External Radiative Efficiency. *ACS Energy Lett.* **2018**, *3*, 2086–2093.

(14) Jiang, Y.; Cui, M.; Li, S.; Sun, C.; Huang, Y.; Wei, J.; Zhang, L.; Lv, M.; Qin, C.; Liu, Y.; Yuan, M. Reducing the Impact of Auger Recombination in Quasi-2D Perovskite Light-Emitting Diodes. *Nat. Commun.* **2021**, *12*, 336.

(15) Chen, P.; Bai, Y.; Lyu, M.; Yun, J.-H.; Hao, M.; Wang, L. Progress and Perspective in Low-Dimensional Metal Halide Perovskites for Optoelectronic Applications. *Sol. RRL* **2018**, *2*, 1700186.

(16) Krishna, A.; Gottis, S.; Nazeeruddin, M. K.; Sauvage, F. Mixed Dimensional 2D/3D Hybrid Perovskite Absorbers: The Future of Perovskite Solar Cells? *Adv. Funct. Mater.* **2019**, *29*, 1806482.

(17) Smith, I. C.; Hoke, E. T.; Solis-Ibarra, D.; McGehee, M. D.; Karunadasa, H. I. A Layered Hybrid Perovskite Solar-Cell Absorber with Enhanced Moisture Stability. *Angew. Chem., Int. Ed.* **2014**, *53*, 11232–11235.

(18) Mitzi, D. B.; Feild, C. A.; Harrison, W. T. A.; Guloy, A. M. Conducting Tin Halides with a Layered Organic-Based Perovskite Structure. *Nature* **1994**, *369*, 467–469.

(19) Saparov, B.; Mitzi, D. B. Organic–Inorganic Perovskites: Structural Versatility for Functional Materials Design. *Chem. Rev.* **2016**, *116*, 4558–4596.

(20) Li, N.; Zhu, Z.; Chueh, C.-C.; Liu, H.; Peng, B.; Petrone, A.; Li, X.; Wang, L.; Jen, A. K.-Y. Mixed Cation $FA_xPEA_{1-x}PbI_3$ with Enhanced Phase and Ambient Stability toward High-Performance Perovskite Solar Cells. *Adv. Energy Mater.* **2017**, *7*, 1601307.
(21) Lee, D. S.; Yun, J. S.; Kim, J.; Soufiani, A. M.; Chen, S.; Cho, Y.; Deng, X.; Seidel, J.; Lim, S.; Huang, S.; Ho-Baillie, A. W. Y. Passivation of Grain Boundaries by Phenethylammonium in Formamidinium-Methylammonium Lead Halide Perovskite Solar Cells. *ACS Energy Lett.* **2018**, *3*, 647−654.
(22) Cho, K. T.; Grancini, G.; Lee, Y.; Oveisi, E.; Ryu, J.; Almora, O.; Tschumi, M.; Schouwink, P. A.; Seo, G.; Heo, S.; Park, J.; Jang, J.; Paek, S.; Garcia-Belmonte, G.; Nazeeruddin, M. K. Selective Growth of Layered Perovskites for Stable and Efficient Photovoltaics. *Energy Environ. Sci.* **2018**, *11*, 952−959.
(23) Kumawat, N. K.; Liu, X.-K.; Kabra, D.; Gao, F. Blue Perovskite Light-Emitting Diodes: Progress, Challenges and Future Directions. *Nanoscale* **2019**, *11*, 2109−2120.
(24) Tennyson, E. M.; Doherty, T. A. S.; Stranks, S. D. Heterogeneity at multiple length scales in halide perovskite semiconductors. *Nat. Rev. Mater.* **2019**, *4*, 573−587.
(25) Quan, L. N.; Yuan, M.; Comin, R.; Voznyy, O.; Beauregard, E. M.; Hoogland, S.; Buin, A.; Kirmani, A. R.; Zhao, K.; Amassian, A.; Kim, D. H.; Sargent, E. H. Ligand-Stabilized Reduced-Dimensionality Perovskites. *J. Am. Chem. Soc.* **2016**, *138*, 2649−2655.
(26) Zheng, Y.; Niu, T.; Ran, X.; Qiu, J.; Li, B.; Xia, Y.; Chen, Y.; Huang, W. Unique Characteristics of 2D Ruddlesden−Popper (2DRP) Perovskite for Future Photovoltaic Application. *J. Mater. Chem. A* **2019**, *7*, 13860−13872.
(27) Wang, N.; Cheng, L.; Ge, R.; Zhang, S.; Miao, Y.; Zou, W.; Yi, C.; Sun, Y.; Cao, Y.; Yang, R.; Wei, Y.; Guo, Q.; Ke, Y.; Yu, M.; Jin, Y.; Liu, Y.; Ding, Q.; Di, D.; Yang, L.; Xing, G.; Tian, H.; Jin, C.; Gao, F.; Friend, R. H.; Wang, J.; Huang, W. Perovskite Light-Emitting Diodes Based on Solution-Processed Self-Organized Multiple Quantum Wells. *Nat. Photonics* **2016**, *10*, 699−704.
(28) Yuan, M.; Quan, L. N.; Comin, R.; Walters, G.; Sabatini, R.; Voznyy, O.; Hoogland, S.; Zhao, Y.; Beauregard, E. M.; Kanjanaboos, P.; Lu, Z.; Kim, D. H.; Sargent, E. H. Perovskite Energy Funnels for Efficient Light-Emitting Diodes. *Nat. Nanotechnol.* **2016**, *11*, 872−877.
(29) Yun, J. S.; Seidel, J.; Kim, J.; Soufiani, A. M.; Huang, S.; Lau, J.; Jeon, N. J.; Seok, S. I.; Green, M. A.; Ho-Baillie, A. Critical Role of Grain Boundaries for Ion Migration in Formamidinium and Methylammonium Lead Halide Perovskite Solar Cells. *Adv. Energy Mater.* **2016**, *6*, 1600330.
(30) Kim, D.; Yun, J.-H.; Lyu, M.; Kim, J.; Lim, S.; Yun, J. S.; Wang, L.; Seidel, J. Probing Facet-Dependent Surface Defects in $MAPbI_3$ Perovskite Single Crystals. *J. Phys. Chem. C* **2019**, *123*, 14144−14151.
(31) Ahmadi, M.; Collins, L.; Higgins, K.; Kim, D.; Lukosi, E.; Kalinin, S. V. Spatially Resolved Carrier Dynamics at $MAPbBr_3$ Single Crystal−Electrode Interface. *ACS Appl. Mater. Interfaces* **2019**, *11*, 41551−41560.
(32) You, J.; Yang, Y.; Hong, Z.; Song, T.-B.; Meng, L.; Liu, Y.; Jiang, C.; Zhou, H.; Chang, W.-H.; Li, G.; Yang, Y. Moisture Assisted Perovskite Film Growth for High Performance Solar Cells. *Appl. Phys. Lett.* **2014**, *105*, 183902.
(33) Mosconi, E.; Azpiroz, J. M.; De Angelis, F. Ab Initio Molecular Dynamics Simulations of Methylammonium Lead Iodide Perovskite Degradation by Water. *Chem. Mater.* **2015**, *27*, 4885−4892.
(34) Kim, D.; Yun, J. S.; Sharma, P.; Lee, D. S.; Kim, J.; Soufiani, A. M.; Huang, S.; Green, M. A.; Ho-Baillie, A. W. Y.; Seidel, J. Light- and Bias-Induced Structural Variations in Metal Halide Perovskites. *Nat. Commun.* **2019**, *10*, 444.
(35) Lei, L.; Seyitliyev, D.; Stuard, S.; Mendes, J.; Dong, Q.; Fu, X.; Chen, Y. A.; He, S.; Yi, X.; Zhu, L.; Chang, C. H.; Ade, H.; Gundogdu, K.; So, F. Efficient Energy Funneling in Quasi-2D Perovskites: From Light Emission to Lasing. *Adv. Mater.* **2020**, *32*, 1906571.
(36) He, M.; Li, B.; Cui, X.; Jiang, B.; He, Y.; Chen, Y.; O'Neil, D.; Szymanski, P.; Ei-Sayed, M. A.; Huang, J.; Lin, Z. Meniscus-Assisted Solution Printing of Large-Grained Perovskite Films for High-Efficiency Solar Cells. *Nat. Commun.* **2017**, *8*, 16045.
(37) Baldan, A. Review Progress in Ostwald Ripening Theories and Their Applications to Nickel-Base Superalloys Part I: Ostwald Ripening Theories. *J. Mater. Sci.* **2002**, *37*, 2171−2202.
(38) Yun, J. S.; Ho-Baillie, A.; Huang, S.; Woo, S. H.; Heo, Y.; Seidel, J.; Huang, F.; Cheng, Y.-B.; Green, M. A. Benefit of Grain Boundaries in Organic−Inorganic Halide Planar Perovskite Solar Cells. *J. Phys. Chem. Lett.* **2015**, *6*, 875−880.
(39) Kim, H.; Choi, M.-J.; Suh, J. M.; Han, J. S.; Kim, S. G.; Le, Q. V.; Kim, S. Y.; Jang, H. W. Quasi-2D Halide Perovskites for Resistive Switching Devices with ON/OFF Ratios Above 109. *NPG Asia Mater.* **2020**, *12*, 21.
(40) Pandey, R.; Vats, G.; Yun, J.; Bowen, C. R.; Ho-Baillie, A. W. Y.; Seidel, J.; Butler, K. T.; Seok, S. I. Mutual Insight on Ferroelectrics and Hybrid Halide Perovskites: A Platform for Future Multifunctional Energy Conversion. *Adv. Mater.* **2019**, *31*, 1807376.
(41) Lee, J.-W.; Bae, S.-H.; De Marco, N.; Hsieh, Y.-T.; Dai, Z.; Yang, Y. The Role of Grain Boundaries in Perovskite Solar Cells. *Mater. Today Energy* **2018**, *7*, 149−160.
(42) Castro-Méndez, A.-F.; Hidalgo, J.; Correa-Baena, J.-P. The Role of Grain Boundaries in Perovskite Solar Cells. *Adv. Energy Mater.* **2019**, *9*, 1901489.
(43) Kim, D.; Higgins, K.; Ahmadi, M. Navigating Grain Boundaries in Perovskite Solar Cells. *Matter* **2021**, *4*, 1442−1445.
(44) Song, J.; Zhou, Y.; Padture, N. P.; Huey, B. D. Anomalous 3D Nanoscale Photoconduction in Hybrid Perovskite Semiconductors Revealed by Tomographic Atomic Force Microscopy. *Nat. Commun.* **2020**, *11*, 3308.
(45) Hermes, I. M.; Bretschneider, S. A.; Bergmann, V. W.; Li, D.; Klasen, A.; Mars, J.; Tremel, W.; Laquai, F.; Butt, H.-J.; Mezger, M.; Berger, R.; Rodriguez, B. J.; Weber, S. A. L. Ferroelastic Fingerprints in Methylammonium Lead Iodide Perovskite. *J. Phys. Chem. C* **2016**, *120*, 5724−5731.
(46) Liu, Y.; Collins, L.; Proksch, R.; Kim, S.; Watson, B. R.; Doughty, B.; Calhoun, T. R.; Ahmadi, M.; Ievlev, A. V.; Jesse, S.; Retterer, S. T.; Belianinov, A.; Xiao, K.; Huang, J.; Sumpter, B. G.; Kalinin, S. V.; Hu, B.; Ovchinnikova, O. S. Chemical Nature of Ferroelastic Twin Domains in $CH_3NH_3PbI_3$ Perovskite. *Nat. Mater.* **2018**, *17*, 1013−1019.
(47) Liu, Y.; Borodinov, N.; Lorenz, M.; Ahmadi, M.; Kalinin, S. V.; Ievlev, A. V.; Ovchinnikova, O. S. Hysteretic Ion Migration and Remanent Field in Metal Halide Perovskites. *Adv. Sci.* **2020**, *7*, 2001176.

https://doi.org/10.1021/acsami.1c07876
ACS Appl. Mater. Interfaces XXXX, XXX, XXX−XXX